Morphology of Weak Lensing Convergence Maps

D. Munshi[a], T. Namikawa[b], J. D. McEwen[a], T. D. Kitching[a], F. R. Bouchet[c]

[a] *Mullard Space Science Laboratory, University College London, Holmbury St Mary, Dorking, Surrey RH5 6NT, UK*
[b] *Department of Applied Mathematics and Theoretical Physics, University of Cambridge, Wilberforce Road, Cambridge CB3 0WA, UK*
[c] *Institut d'Astrophysique de Paris, UMR 7095, CNRS & Sorbonne Universit, 98 bis Boulevard Arago, F-75014 Paris, France*

13 October 2020

ABSTRACT

We study the morphology of convergence maps by perturbatively reconstructing their Minkowski Functionals (MFs). We present a systematics study using a set of three *generalised* skew-spectra as a function of source redshift and smoothing angular scale. Using an approach based on pseudo-S_ℓs (PSL) we show how these spectra will allow reconstruction of MFs in the presence of an arbitrary mask and inhomogeneous noise in an unbiased way. Our theoretical predictions are based on a recently introduced fitting function to the bispectrum. We compare our results against state-of-the art numerical simulations and find an excellent agreement. The reconstruction can be carried out in a controlled manner as a function of angular harmonics ℓ and source redshift z_s which allows for a greater handle on any possible sources of non-Gaussianity. Our method has the advantage of estimating the topology of convergence maps directly using shear data. We also study weak lensing convergence maps inferred from Cosmic Microwave Background (CMB) observations; and we find that, though less significant at low redshift, the *post-Born corrections* play an important role in any modelling of the non-Gaussianity of convergence maps at higher redshift. We also study the cross-correlations of estimates from different tomographic bins.

Key words: : Cosmology– Weak Lensing– Methods: analytical, statistical, numerical

1 INTRODUCTION

The recently completed Cosmic Microwave Background (CMB) experiments such as the Planck Surveyors[1](Planck Collaboration 2014, 2018) has provided us a standard model of cosmology. However, many of the outstanding questions including, e.g., but not limited to, the nature of dark matter (DM) and dark energy (DE) as well as possible modification of General Relativity (GR) on cosmological scales (Joyce et al. 2015; Clifton et al. 2016) or the exact nature of neutrino mass hierarchy (Planck Collaboration 2016) still remains unclear. The significant increase in precision achieved by stage-IV CMB and large scale structure surveys will allow us to answer some of these questions. It is expected that the ongoing weak lensing surveys Canada-France-Hawaii Telescope (CFHTLS[2]), Dark Energy Surveys[3](Abott et al. 2015) , Dark Energy Spectroscopic Instruments[4], Prime Focus Spectrograph[5], Kilo-Degree Survey (KIDS,

---

[1] http://http://sci.esa.int/planck/
[2] http://www.cfht.hawai.edu/Sciences/CFHLS
[3] https://www.darkenergysurvey.org/
[4] http://desi.lbl.gov
[5] http://pfs.ipmu.jp

Kuijken (2015)) and stage-IV large scale structure (LSS) surveys such as *Euclid*[6](Laureijis et al. 2011), Rubin Observatory[7](Tyson et al. 2003), Roman Space Telescope(National Research Council 2010) will provide answers to many of the questions that cosmology is facing.

Weak lensing is responsible for the minute shearing and magnification in the images of the distant galaxies by the intervening large-scale structure allow us to extract information about clustering of the intervening mass distribution in the Universe (Mandelbaum 2018; Kilbinger 2015; Munshi et al. 2008; Bartelmann & Schneider 2001). Weak lensing also leaves its imprints on the observed CMB sky. The weak lensing surveys are complementary to the galaxy surveys such as Baryon Oscillation Spectroscopic Survey[8](Eisenstein et al. 2015), Extended Baryon Oscillation Spectroscopic Survey(eBOSS Collaboration 2020) or WiggleZ[9](Abott et al. 2015) as they provide an unbiased picture of the underlying dark matter distribution whereas the galaxies and other tracers can only provide a biased picture (Desjacques, Jeong, Schmidt 2015).

However, weak lensing observations are sensitive to small scales where clustering is nonlinear and non-Gaussian (Bernardeau et al. 2002). Indeed, the statistical estimates of cosmological parameters based on power spectrum analysis is typically degenerate in cosmological parameter, e.g., σ_8 and Ω_M. External data sets, e.g., CMB as well as tomographic or 3D (Castro, Heavens, Kitching 2005) information is typically used to lift the degeneracy. However, an alternative procedure would be to use high-order statistics of observables that probe the nonlinear regime(Munshi et al. 2011; Munshi, Heavens, Coles 2011; Munshi et al. 2015). Even in the absence of any primordial non-Gaussianity, the gravitational clustering induces mode coupling that results in a secondery non-Gaussianity which is more pronounced at the smaller scales where weak lensing surveys are sensitive. Thus a considerable amount of effort has been invested in understanding the gravity induced secondary non-Gaussianity from weak lensing surveys. These statistics include the lower order cumulants (Munshi & Jain 2001) and their correlators (Munshi 2000); the multispectra including the skew-spectrum (Munshi & Heavens 2010) and kurtosis spectra (Munshi et al. 2011) as well as the entire PDF (Munshi & Jain 2000) and the statistics of hot and cold spots. The future surveys such as the *Euclid* survey will be particularly interesting in this regard. With its large fraction of sky-coverage it will be able to detect the gravity induced non-Gaussianity with a very high signal-to-noise (S/N). It is also worth mentioning here that, in addition to breaking the degeneracy in cosmological parameters the higher-order statistics is also important in understanding the covariance of lower-order estimators. (Valageas, Munshi, Barber 2005; Munshi, Valageas, Barber 2004; Barber, Munshi, Valageas 2004; Valageas, Barber, Munshi 2010)

Topological estimators such as the Minkowski Functionals (MFs) are also important diagnostics in this direction as they carry information at all-order. The MFs have been extensively developed as a statistical tool in a cosmological setting for both 2-dimensional (projected) and 3-dimensional (redshift) surveys. The MFs have analytically known results for a Gaussian random field making them suitable for studies of non-Gaussianity. Examples of such studies include CMB data (Natoli et al. (2010); Hikage et al. (2008); Novikov, Schmalzing and Mukhanov (2000); Schmalzing & Górski (1998); Ducout et al. (2013); Planck Collaboration (2016, 2019)), large scale structure (Gott et al. (1986); Coles (1988); Gott et al. (1989); Melott (1990); Moore et al. (1992); Gott et al. (1992); Canavezes et al. (1998); Schmalzing & Diaferio (2000); Kerscher et al. (2001); Park et al. (2005); Hikage et al. (2008); Hikage, Komatsu & Mastubara (2006); Hikage et al. (2002)), weak lensing (Matsubara and Jain (2001); Sato et al. (2001); Taruya et al. (2002); Munshi et al. (2011)), Sunyaev-Zel'dovich (SZ) maps (Munshi et al. 2011), 21cm (Gleser et al. (2006)) and N-body simulations (Schmalzing & Diaferio (2000); Kerscher et al. (2001)). Note that this is an incomplete list of references and we have selected a sample of representative papers from the literature. The MFs are spatially defined topological statistics and, by definition, contain statistical information of all orders. This makes them complementary to the polyspectra methods that are defined in Fourier space. It is also possible that the two approaches will be sensitive to different aspects of non-Gaussianity and systematic effects although in the weakly non-Gaussian limit it has been shown that the MFs reduce to a weighted probe of the bispectrum (Hikage, Komatsu & Mastubara (2006)). In addition to providing cosmological information, MFs can also be useful diagonistics of any unknown systematics as well as baryonic contamination which are expected to affect weak lensing observables (Herenois-Deraps 2016).

This paper is organised as follows. The Minkowski Functionals are reviewed in §2. Our notations for the weak lensing statistics in projection are described in §3. The generalised skew-spectra are expressed in terms of the bispectrum in §4. The fitting function we use for our reconstruction is described in §5. A very brief description of the simulations is provided in §6. We discuss the results in §7. The conclusions are presented in §8.

---

2 MINKOWSKI FUNCTIONALS

The MFs are related to Hadwiger's theorem Hadwiger (1959) in integral geometry framework which asserts that a set of $d+1$ functionals can provide all necessary information of a random field in d-dimensional space. These functionals are a unique set of morphological estimators that are *motion-invariant* and obey properties such as *convex-continuity* as well as *additivity*. These properties are important for computing morphological estimators from a pixelized map. The MFs are defined over an excursion set Σ for a given threshold ν and are expressed in terms of weighted curvature integrals.

In two dimension (2D) the three MFs are defined and can be expressed using the following notations of Hikage et al. (2008):

$$V_0(\nu) = \int_\Sigma da; \quad V_1(\nu) = \frac{1}{4}\int_{\partial\Sigma} dl; \quad V_2(\nu) = \frac{1}{2\pi}\int_{\partial\Sigma} \mathcal{K} dl. \tag{1}$$

Following the standard notation in cosmological literature, we use da, dl to denote the surface area and line elements for an excursion set Σ and its boundary $\partial\Sigma$ respectively that crosses a threshold. The MFs $V_k(\nu)$ correspond to the area of the excursion set Σ, the length of its boundary $\partial\Sigma$ as well as the integral of curvature $\mathcal{K}$ along its boundary which is also related to the genus g and hence the Euler characteristics χ.

The Minkowski Functionals can be employed to quantify deviations from Gaussianity. At leading order the MFs can be constructed completely from the knowledge of the bispectrum alone.

The behaviour of the MFs for a random Gaussian field is well known and is given by Tomita's formula (Tomita 1986). The MFs are denoted by $V_k(\nu)(k = 0, 1, 2)$ for a threshold $\nu = \kappa/\sigma_0$, where $\sigma_0^2 = \langle\kappa^2\rangle$ can be decomposed into two different contributions, Gaussian $V_k^G(\nu)$ and perturbative non-Gaussian contribution $\delta V_k(\nu)$:

$$V_k(\nu) = V_k^G(\nu) + \delta V_k(\nu). \tag{2}$$

We are primarily interested in the gravity induced non-Gaussian contribution, i.e. $\delta V_k(\nu)$ (Hikage et al. 2008),

$$V_k^G(\nu) = A \exp\left(-\frac{\nu^2}{2}\right) H_{k-1}(\nu); \tag{3}$$

$$\delta V_k(\nu) = A \exp\left(-\frac{\nu^2}{2}\right) \left[\delta V_k^{(2)}(\nu)\sigma_0 + \delta V_k^{(3)}(\nu)\sigma_0^2 + \delta V_k^{(4)}(\nu)\sigma_0^3 + \cdots\right]. \tag{4}$$

where $H_k(\nu)$ is the Hermite polynomials. Following the notations introduced in Hikage et al. (2008) we have separated out a normalisation factor A in these expressions which is given by the generalised variance parameter σ_0^2 and σ_1^2:

$$A = \frac{1}{(2\pi)^{(k+1)/2}} \frac{\omega_2}{\omega_{2-k}\omega_k} \left(\frac{\sigma_1}{\sqrt{2}\sigma_0}\right)^k. \tag{5}$$

Here, $\omega_k = \pi^{k/2}/\Gamma(k/2+1)$ is the volume of a k-dimensional unit ball. For projected weak lensing convergence maps in 2D we only need $\omega_0 = 1$, $\omega_1 = 2$ and $\omega_2 = \pi$. The coefficient depend only on the power spectrum of the perturbation through σ_0 and σ_1. These quantites are defined through the following expression:

$$\sigma_j^2 = \frac{1}{2\pi}\sum_\ell [\ell(\ell+1)]^j (2l+1)\mathcal{C}_\ell W_\ell^2. \tag{6}$$

Here $\mathcal{C}_\ell$ is the angular power spectrum of the underlying field and W_ℓ is the window function used to smooth a map. A more through discussion will be presenetd in the follwoing section for κ maps. At the level of the bispectrum the perturbative corrections are determined by three generalised skewness paramters $S^{(k)}$ (Hikage et al. 2008):

$$\delta V_k^{(2)}(\nu) = \left[\left\{\frac{1}{6}S^{(0)}H_{k+2}(\nu) + \frac{k}{3}S^{(1)}H_k(\nu) + \frac{k(k-1)}{6}S^{(2)}H_{k-2}(\nu)\right\}\right]; \tag{7}$$

The skewness parameters can also be expressed as (Munshi et al. 2011):

$$S^{(0)} = \frac{\langle\kappa^3\rangle}{\sigma_0^2}; \quad S^{(1)} = \frac{\langle\kappa^2\nabla^2\kappa\rangle}{\sigma_0^2\sigma_1^2}; \quad S^{(2)} \equiv \frac{\langle|\nabla\kappa|^2\nabla^2\kappa\rangle}{\sigma_1^2}. \tag{8}$$

Here, $S^{(0)}$ is the ordinary skewness parameter where as $S^{(1)}$ and $S^{(2)}$ are its higher-order generalisations. At next order a set of four

kurtosis parameters can be used to expressed the next-order correlations (Munshi et al. 2011). The primary motivation of this article is to reconstruct these generalised skewness parameters using spectra associated with them that allows to estimate them from surveys in the presence of complicated mask and noise. We will borrow the analytical tools developed in (Munshi et al. 2011).

3   WEAK LENSING POWER SPECTRUM AND BISPECTRUM

The weak lensing convergence denoted as κ can be expressed in terms of a line-of-sight (los) integration of three-dimensional (3D) density contrast δ

$$\kappa(\boldsymbol{\theta}, r_s) = \int_o^{r_s} dr\, \omega(r, r_s)\delta(\boldsymbol{\theta}, r); \quad \omega(r, r_s) = \frac{3}{2}\frac{H_0^2}{a\, c^2}\Omega_M \frac{d_A(r - r_s)}{d_A(r)d_A(r_s)}; \tag{9}$$

In our notation $r = |\boldsymbol{r}|$ denotes the *comoving* radial distance to the source and $\boldsymbol{\theta}$ denotes the angular position on the sky, The background cosmology is specified in terms of Ω_{M} which denotes the cosmological matter density parameter (that describes the total matter density in units of the critical density), H_0 which denotes the Hubble constant; c is the speed of light, and $a = 1/(1 + z)$ denotes the scale factor at a redshift z. The comoving angular diameter distance at a comoving radial distance r is represented as $d_A(r)$. The source plane is assumed to be at a redshift z_s, or equivalently at comoving radial distance r_s. To simplify the analysis we will ignore source distribution and photometric redshift errors. We will focus on the morphological estimators as a function as a function of z_s.

For the smoothed convergence κ, the mean is zero, $\langle \kappa(\boldsymbol{\theta}) \rangle = 0$, and using a spherical harmonic decomposition of $\kappa(\boldsymbol{\theta})$, using spherical harmonics $Y_{\ell m}(\boldsymbol{\theta})$ as the basis functions, $\kappa(\boldsymbol{\theta}) = \sum_{\ell m} \kappa_{\ell m} Y_{\ell m}(\boldsymbol{\theta})$, we can define its angular power spectrum $\mathcal{C}_l$ in terms of the harmonic coefficients $\kappa_{\ell m}$ $\langle \kappa_{\ell m}\kappa^*_{\ell' m'} \rangle = \mathcal{C}_\ell \delta_{\ell\ell'}\delta_{mm'}$ which is a sufficient statistical characterization of a Gaussian field.

$$\mathcal{C}_\ell = \int_0^{r_s} dr \frac{w^2(r, r_s)}{d_A^2(r)} P\left(\frac{\ell}{d_A(r)}; r\right). \tag{10}$$

The convergence bispectrum $\mathcal{B}$ can likewise be expressed using the following los integration of the bispectrum of the density contrast δ denoted as B_δ (see (Munshi et al. 2008)):

$$\langle \kappa_{\ell_1 m_1}\kappa_{\ell_2 m_2}\kappa_{\ell_3 m_3} \rangle_c \equiv \mathcal{B}_{\ell_1\ell_2\ell_3}\left(\begin{array}{ccc} \ell_1 & \ell_2 & \ell_3 \\ m_1 & m_2 & m_3 \end{array} \right). \tag{11}$$

The matrix above represents a Wigner 3j symbol and the angular brackets here represent ensemble averaging. The angular brackets represent ensemble averaging. This particular form is employed as it preserves the the rotational invariance of the three-point correlation function.

The Wigner $3j$-symbol, which is nonzero only when the triplets (ℓ_1, ℓ_2, ℓ_3) satisfy the *triangularity* condition $|\ell_1 - \ell_2| \le \ell_3 \le \ell_1 + \ell_2$ as well as the condition that the sum $\ell_1 + \ell_2 + \ell_3$ is even. This ensures the parity invariance of the bispectrum and neglect presence of any parity violating physics. This selection rule is imposed by the invariance of the field under spatial inversion. Indeed, the parity violating contributions at the level of the bispectrum can be obtained by including both the (so-called) Electric (E) and Magnetic (B) modes (Munshi et al. 2011). This can be used to detect any possible parity violating physics as well as other systematic effects.

The convergence bispectrum $\mathcal{B}$ is expressed in terms of the bispectrum for the density contrast: B:

$$\mathcal{B}_{\ell_1\ell_2\ell_3} = I_{\ell_1\ell_2\ell_3}\int_0^{r_s} dr \frac{w^3(r, r_s)}{d_A^4(r)} B\left(\frac{\ell_1}{d_A(r)}, \frac{\ell_2}{d_A(r)}, \frac{\ell_3}{d_A(r)}; r\right) \tag{12}$$

$$I_{\ell_1\ell_2\ell_3} = \sqrt{\frac{(2\ell_1 + 1)(2\ell_2 + 1)(2\ell_3 + 1)}{4\pi}}\left(\begin{array}{ccc} \ell_1 & \ell_2 & \ell_3 \\ 0 & 0 & 0 \end{array} \right). \tag{13}$$

The cross-spectrum $\mathcal{C}_\ell^{\alpha\beta}$ and mixed bispectrum $\mathcal{B}_{\ell_1\ell_2\ell_3}^{\alpha\beta}$ involving two topographic bins α and β have the following form:

$$\mathcal{C}_\ell^{\alpha\beta} = \int_0^{r_{\min}} dr \frac{\omega_\alpha(r)\omega_\beta(r)}{d_A^2(r)} P\left(\frac{l}{d_A(r)}; r\right); \tag{14a}$$

$$\mathcal{B}_{\ell_1\ell_2\ell_3}^{\alpha\beta} = I_{\ell_1\ell_2\ell_3}\int_0^{r_{\min}} dr \frac{\omega_\alpha^1(r)\omega_\beta^2(r)}{d_A^4(r)} B\left(\frac{\ell_1}{d_A(r)}, \frac{\ell_2}{d_A(r)}, \frac{\ell_3}{d_A(r)}; r\right); \quad r_{min} = min(r_\alpha, r_\beta); \tag{14b}$$

$$w_i(r) := \frac{3\Omega_{\mathrm{M}}}{2}\frac{H_0^2}{c^2}a^{-1}\frac{d_A(r)d_A(r_{si} - r)}{d_A(r_{si})}; \quad i \in \{\alpha, \beta\}. \tag{14c}$$

Using these expression we will next construct the generalised skew-spectra that are useful in constructing the MFs.

4 GENERALISED SKEW-SPECTRA

Individual triplets of harmonics (ℓ_1, ℓ_2, ℓ_3) defines a triangle in the harmonic domain and specify a bispectral mode. The skew-spectra defined below are summed over all possible configuration of the bispectrum by keeping one side of the triangle fixed. Following (Munshi et al. 2011) we introduce the generalised skew-spectra $S_\ell^{(i)}$:

$$S_\ell^{(0)} = \frac{1}{12\pi\sigma_0^4} \frac{1}{2\ell+1} \sum_m \text{Real}\{[\kappa^2]_{\ell m}[\kappa]_{\ell m}^*\} = \frac{1}{12\pi\sigma_0^4} \sum_{\ell_1\ell_2} \mathcal{B}_{\ell\ell_1\ell_2} J_{\ell\ell_1\ell_2} W_\ell W_{\ell_1} W_{\ell_2}; \tag{15a}$$

$$S_\ell^{(1)} = \frac{1}{16\pi\sigma_0^2\sigma_1^2} \frac{1}{2\ell+1} \sum_m \text{Real}\{[\kappa^2]_{\ell m}\nabla^2[\kappa]_{\ell m}^*\} = \frac{1}{16\pi\sigma_0^2\sigma_1^2} \ell(\ell+1) \sum_{\ell_i} \mathcal{B}_{\ell\ell_1\ell_2} J_{\ell\ell_1\ell_2} W_\ell W_{\ell_1} W_{\ell_2}; \tag{15b}$$

$$S_\ell^{(2)} = \frac{1}{8\pi\sigma_1^4} \frac{1}{2\ell+1} \sum_m \text{Real}\{[\nabla\kappa \cdot \nabla\kappa]_{\ell m}[\kappa^2]_{\ell m}^*\}$$

$$= \frac{1}{8\pi\sigma_1^4} \sum_{\ell_i} \Big[[\ell(\ell+1) + \ell_1(\ell_1+1) - \ell_2(\ell_2+1)]\ell_2(\ell_2+1) \Big] \mathcal{B}_{\ell\ell_1\ell_2} J_{\ell\ell_1\ell_2} W_\ell W_{\ell_1} W_{\ell_2}. \tag{15c}$$

We have introduced the following notations above:

$$J_{\ell_1\ell_2\ell_3} \equiv \frac{I_{\ell_1\ell_2\ell_3}}{2\ell_3+1} = \sqrt{\frac{(2\ell_1+1)(2\ell_2+1)}{(2\ell_3+1)4\pi}} \begin{pmatrix} \ell_1 & \ell_2 & \ell_3 \\ 0 & 0 & 0 \end{pmatrix}; \tag{15d}$$

$$W_\ell = \exp\left[-\ell(\ell+1)\frac{\theta_s^2}{8\ln 2} \right]. \tag{15e}$$

We will study these spectra using numerical simulations and test them against theoretical predictions that rely on a fitting function based approach. We will use a Gaussian window function W_ℓ in our study but the expressions are valid for arbitrary window function, including the tophat or compensated window (filter) functions. The one-point skewness parameters $S^{(i)}$ can be recovered from their respective skew-spectra, which were used in Eq.(8):

$$S^{(i)} = \frac{1}{4\pi} \sum_l (2\ell+1) S_\ell^{(i)}. \tag{16}$$

Expressions for the skew-spectra in Eq.(15a)-Eq.(15c) can also be generalised to include cases where instead of individual bins two different bins are cross-correlated.

$$S_\ell^{(0)\alpha\beta} = \frac{1}{2\ell+1} \sum_m \text{Real}\{[\kappa_\alpha^2]_{\ell m}[\kappa_\beta]_{\ell m}^*\} = \frac{1}{12\pi\sigma_0^4} \sum_{\ell_1\ell_2} \mathcal{B}_{\ell\ell_1\ell_2}^{\alpha\beta} J_{\ell\ell_1\ell_2} W_\ell W_{\ell_1} W_{\ell_2}. \tag{17}$$

Similar expressions can be obtained for the other skew-spectra by replacing $\mathcal{B}_{\ell\ell_1\ell_2}$ by $\mathcal{B}_{\ell\ell_1\ell_2}^{\alpha\beta}$ in Eq.(15b)-Eq.(15c). The mixed bispectra $\mathcal{B}_{\ell\ell_1\ell_2}^{\alpha\beta}$ is defined in Eq.(14b). Notice that by construction $S_\ell^{(i)\alpha\beta} \neq S_\ell^{(i)\beta\alpha}$ as $\mathcal{B}_{\ell\ell_1\ell_2}^{\alpha\beta} \neq \mathcal{B}_{\ell\ell_1\ell_2}^{\beta\alpha}$.

Although we have adopted an harmonic approach, equivalent information about the non-Gaussianity can also be obtained by studying the corresponding *collapsed* three-point correlation functions. This approach will be more efficient for surveys with smaller sky-coverage and in the presence of a non-trivial mask:

$$S_{12}^{(0)\alpha\beta}(\theta) = \langle \kappa_\alpha^2(\boldsymbol{\theta}_1)\kappa_\beta(\boldsymbol{\theta}_2) \rangle; \quad S_{12}^{(1)\alpha\beta}(\theta) = \langle \kappa_\alpha^2(\boldsymbol{\theta}_1)\nabla^2\kappa_\beta(\boldsymbol{\theta}_2) \rangle; \quad S_{12}^{(2)\alpha\beta}(\theta) = \langle \nabla^2\kappa_\alpha(\boldsymbol{\theta}_1)[\nabla\kappa_\beta(\boldsymbol{\theta}_2) \cdot \nabla\kappa_\beta(\boldsymbol{\theta}_2)] \rangle; \tag{18}$$

Due to the isotropy and homogeneity of the background Universe these correlations functions are only function of the separation angle $\theta = |\boldsymbol{\theta}_1 - \boldsymbol{\theta}_2|$. These two-point correlations can be constructed by cross-correlating derived maps from different topographic bins $\kappa_\alpha^2(\boldsymbol{\theta})$, $\nabla^2\kappa_\alpha(\boldsymbol{\theta})$ and $\nabla\kappa_\alpha(\boldsymbol{\theta}) \cdot \nabla\kappa_\alpha(\boldsymbol{\theta})$. In terms of the skew spectra these correlations functions can be expressed as:

$$S_{12}^{(i)\alpha\beta}(\theta) = \frac{1}{4\pi} \sum_\ell (2\ell+1) P_\ell(\cos\theta) S_\ell^{(i)}; \qquad i \in \{0, 1, 2\}. \tag{19}$$
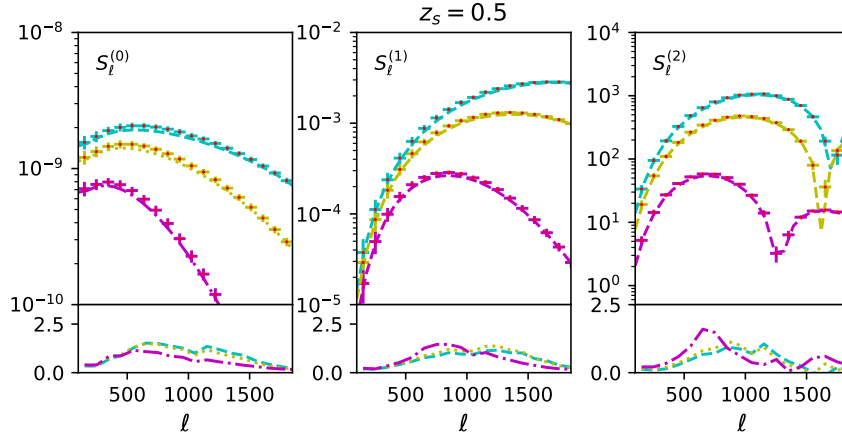
Figure 1. From left to right different panels depict the skew-spectra S_ℓ^0, $S_\ell^{(1)}$ and $S_\ell^{(1)}$ respectively as a function of ℓ. The data points with erro-bars in each panel are the bin-averaged values of the respective skew-spectra estimated from simulations. Different curves in each panel correspond to different smoothing angular scales. These generalised skew-spectra are defined in Eq.(15a)-Eq.(15c). In each panel, three different smoothing angular scales $\theta_s = 2'$, $5'$ and $10'$ (from top to bottom) are shown. The source redshift is fixed at $z_s = 0.5$. A Gaussian smoothing window was used. See text for more details. The bottom subpanels for each panel show the deviation Δ_l of simulations $S_\ell^{\rm sim}$ from theoretical prediction $S_\ell^{\rm th}$ in units of standard deviation σ_ℓ computed for individual beans i.e. $\Delta_\ell = (S_\ell^{\rm th} - S_\ell^{\rm sim})/\sigma_\ell$. No noise or mask were used.
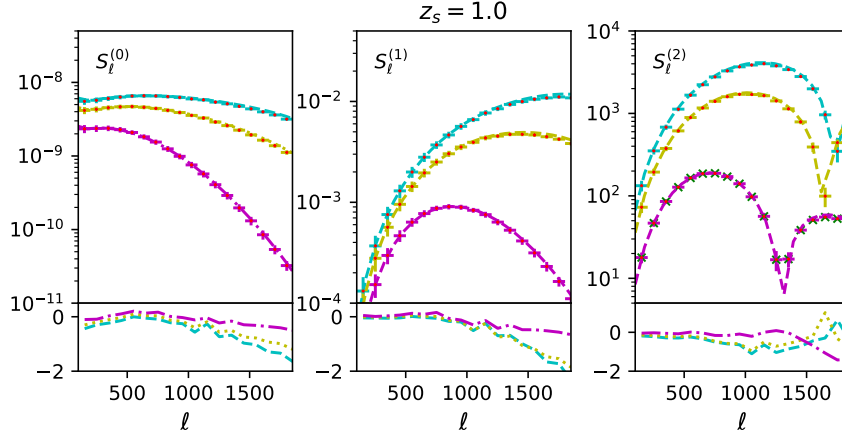
Figure 2. Same as Figure-1, but for $z_s = 1.0$.

Here P_ℓ denotes the Legendre polynomial of order ℓ.

So far we have assumed a full-sky coverage for estimation of the generalised skew-spectra. However, most surveys will have a partial sky-covergage. The pseudo skew-spectrum (PSL) technique presented in (Munshi et al. 2020a) is also valid for the generalised skew-spectra. An unbiased all-sky estimate $\hat{S}_\ell$ can be constructed from the masked skew-spectra $\tilde{S}_\ell$ using the expression below:

$$\tilde{S}_\ell^{(i)} = M_{\ell\ell'}S_\ell^{(i)}; \quad \hat{S}_\ell^{(i)} = M_{\ell\ell'}^{-1}\tilde{S}_\ell^{(i)}; \quad \langle\hat{S}_\ell^{(i)}\rangle = S_\ell^{(i)} \tag{20a}$$

where the mode-coupling (mixing) matrix is given by:

$$M_{\ell\ell'} = (2\ell'+1)\sum_{\ell''}\begin{pmatrix} \ell & \ell' & \ell'' \\ 0 & 0 & 0 \end{pmatrix}^2 \frac{(2\ell''+1)}{4\pi}|w_{\ell''}^2|; \tag{21}$$
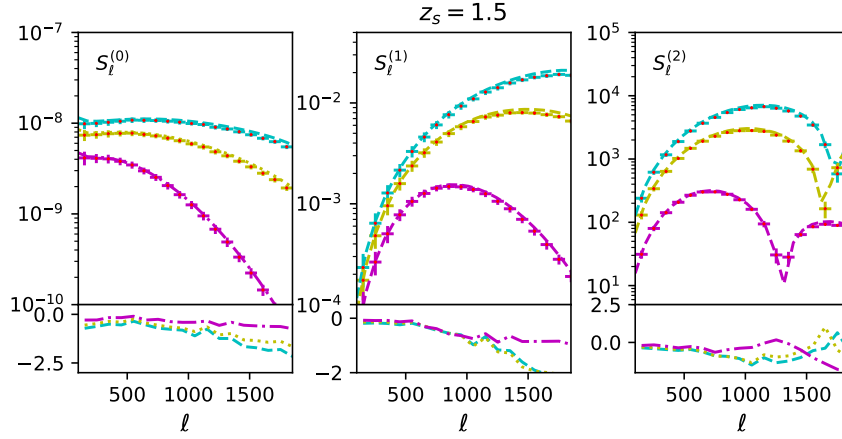
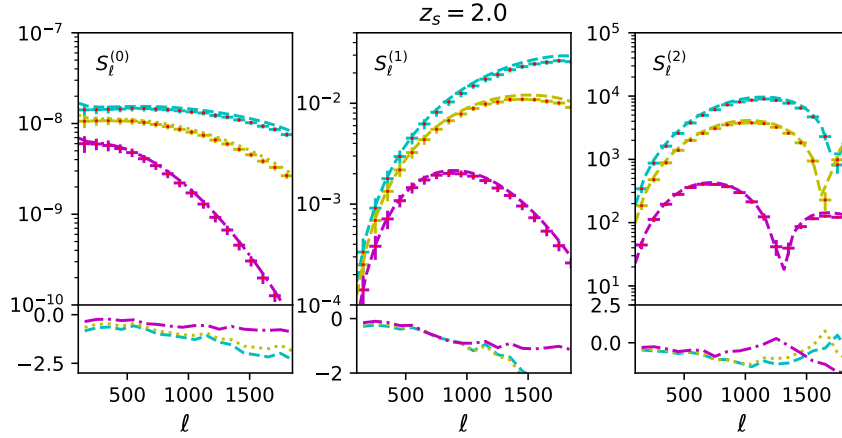**Figure 3.** Same as Figure-1, but for $z_s = 1.5$.

Figure 4. Same as Figure-1, but for $z_s = 2.0$.

Here we have introduced the power spectrum of the mask $w(\boldsymbol{\theta})$, i.e., $w_\ell = 1/(2\ell + 1) \sum_m |w_{\ell m}|^2$, constructed from the harmonic-coefficient $w_{\ell m}$ and its complex conjugate $w_{\ell m}^*$ (see Munshi et al. (2020a) for more detailed discussion) Notice that a (inhomogeneous) Gaussian noise do not contribute to the generalised skew-specra though it will increase the scatter. This PSL method will be essential for constructing morphology of weak lensing κ maps in the presence of a mask with non-trivial topology.

5 FITTING FUNCTION FOR BISPECTRUM

In second-order Eulerian perturbation theory the matter bispectrum $B(\mathbf{k}_1, \mathbf{k}_2, \mathbf{k}_3)$ that encodes mode coupling of the 3D density contrast in the Fourier domain can be expressed as (Bernardeau et al. 2002):

$$B(\mathbf{k}_1, \mathbf{k}_2, \mathbf{k}_3) = 2F_2(\mathbf{k_1}, \mathbf{k_2})P_{lin}(\mathbf{k}_1)P_{lin}(\mathbf{k}_2) + \text{cyc.perm.}. \tag{22a}$$

Here F_2 is the kernel that encapsulates the second-order mode-mode coupling and $P_{lin}(\mathbf{k})$ denotes the linear power spectrum of the density contrast δ. In a fitting function approach the analytical form of the kernel F_2 is generalised from the quasi-linear regime to nonlinear regime by introducing three independent coefficients $a(n_e, k), b(n_e, k)$ and $c(n_e, k)$ that are determined using numerical

simulations.

$$F_2(\mathbf{k_1}, \mathbf{k_2}) = \frac{5}{7} a(n_e, k) a(n_e, k) + \frac{1}{2} \left(\frac{\mathbf{k}_1 \cdot \mathbf{k}_2}{k_2^2} + \frac{\mathbf{k}_1 \cdot \mathbf{k}_2}{k_1^2} \right) b(n_e, k) b(n_e, k) + \frac{2}{7} \left(\frac{\mathbf{k}_1 \cdot \mathbf{k}_2}{k_1 k_2} \right)^2 c(n_e, k) c(n_e, k) \tag{22b}$$

Here n_e is local logarithmic slope of the power spectrum at 3D wavenumber k. In the quasi-linear regime these coefficients approach unity, i.e, $a = b = c = 1$. In the highly nonlinear regime, if we set $a \neq 0$ and $b = c = 0$, we recover the hierarchal form for the matter bispectrum. The idea of a fitting function was initially proposed in (Scoccimarro & Frieman 1999). It interpolates between the perturbative and the nonlinear regimes. It has a limited validity range of $k < 3h\mathrm{Mpc}^{-1}$ and $z \approx 0 - 1$. The functional form of this fitting function was later improved by (Gil-Marin et al. 2012) with a rather limited validity range of $k < 0.4h\mathrm{Mpc}^{-1}$ and $z \approx 1.5$. The improvement was achieved by introducing additional free parameters which are extracted from numerical simulations. The inaccuracy of this fitting function was pointed out by Munshi et al. (2020b). An even more accurate fitting function was recently proposed by (Takahashi et al. 2017). This new fitting function has a validity range of $k < 10h\mathrm{Mpc}^{-1}$ and $z \approx 1 - 3$. Its higher accuracy is important for a very accurate theoretical predictions of secondary non-Gaussianity across the range of wavelength and redshift that will be useful for stage-IV large scale structure experiments including *Euclid*. This function has already been used in (Munshi et al. 2020a). In our study we will use it to compute the theoretical predictions for our morphological estimators.

For modelling of skew-spectrum related to secondary non-Gaussianity, using halo model as well as primordial non-Gaussianity, see (Munshi et al. 2011).

6   SIMULATIONS

In our numerical investigations we use the all-sky weak lensing maps described in (Takahashi et al. 2017)[10]. These maps were generated using ray-tracing through N-body simulations using multiple lens planes and to generate convergence κ as well as shear γ maps. They do not employ the Born approximation. The post-Born corrections are known to play an important role at higher redshifts especially for CMB lensing. The source redshifts used were in the range $z_s = 0.05 - 5.30$ at an interval of $\Delta z_s = 0.05$. We have used the maps corresponding to source redshifts of $z_s = 0.5, 1.0, 1.5, 2.0$ in our study. For generating lensed CMB maps numerical simulations were replaced by Gaussian realisations of density fluctuations in the redshift range $z_s = 7.1 - 1100.0$. The perturbations were generated using a linear matter power spectrum. These maps were generated using different resolution in $\mathtt{HEALPix}$[11] format(Gorski et al. 2016) using an equal area pixelisation scheme. The number of pixels scales as $N_{\mathrm{pix}} = 12 N_{\mathrm{side}}^2$ with the resolution parameter N_{side}. We will be using maps generated at a resolution $N_{\mathrm{side}} = 4096$ and used maps at a higher resolution for various sanity checks. In our study we will be restricting us to $\ell \leq \ell_{\max}$ with $\ell_{\max} = 2000$. However, the $\ell_{\max}$ is kept flexible in our analytical formalism and can be used to filter out any astrophysical complexities related baryonic feedback (Weiss et al. 2019).

The cosmological parameters used are $\Omega_{\mathrm{CDM}} = 0.233$, $\Omega_b = 0.046$, $\Omega_{\mathrm{M}} = \Omega_{\mathrm{CDM}} + \Omega_b$, $\Omega_\Lambda = 1 - \Omega_{\mathrm{M}}$ and $h = 0.7$. For the amplitude of density fluctuation, $\sigma_8 = 0.82$, and the spectral index $n_s = 0.97$ is used. These maps were recently used to analyze the bispectrum in the context of CMB lensing (Namikawa et al. 2018) as well in studies of lensing induced bispectrum in low redshift (Munshi et al. 2020a,b)

7   RESULTS AND DISCUSSION

In this section we will summarize the main results presented in this paper along with their implications.

(i) **Skew-spectra for individual tomographic bins at a low redshift:** In Fig.-1 –4 the generalised skew-spectra $S_\ell^{(0)}$, $S_\ell^{(1)}$ and $S_\ell^{(2)}$ (from left to right) are being plotted as a function of ℓ. These figures correspond to different source redshifts $z_s = 0.5$, $z_s = 1.0$, $z_s = 1.5$ and $z_s = 2.0$ respectively. The various line styles in each panels correspond to different smoothing angular scales. We use a Gaussian window in our study. From top to bottom different curves represent Full Width at Half Maxima (FWHM) of $\theta_s = 2.0'$, $\theta_s = 5.0'$ and $\theta_s = 10.0'$ respectively. We use the noise free simulations described in 6. We have used Eq.(15a)-Eq.(15c) to evaluate the theoretical expectations for $S_\ell^{(0)}$, $S_\ell^{(1)}$, $S_\ell^{(2)}$ along with the fitting function by (Takahashi et al. 2017) discussed in §5. We have used theoretical predictions with and without the post-Born approximation but we find inclusion of such corrections make no significant

---

[10] http://cosmo.phys.hirosaki-u.ac.jp/takahasi/allsky_raytracing/
[11] https://healpix.jpl.nasa.gov/
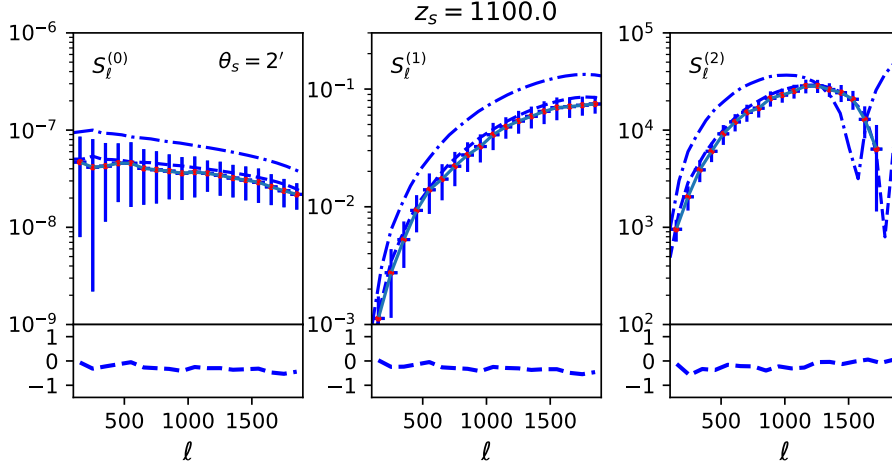
Figure 5. The generalised skew-spectra κ maps are shown for $z_s = 1100$.. From left to right we show results for the skew-spectra $S_\ell^{(0)}$, $S_\ell^{(1)}$ and $S_\ell^{(2)}$ as a function of ℓ. These generalised skew-spectra are defined in Eq.(15a)-Eq.(15c). The κ maps are inferred from CMB temperature maps. The dashed and solid lines represents the theoretical predictions based on Born- and post-Born approximation. The importance of post-Born approximation is more pronounced at higher redshift. The smoothing angular scale is fixed at $\theta_s = 2'$. Results are obtained using one all-sky map. No noise was included. An all-sky coverage was assumed. The error-bars were computed using the scatter within the bin fixed at $\delta\ell = 100$.
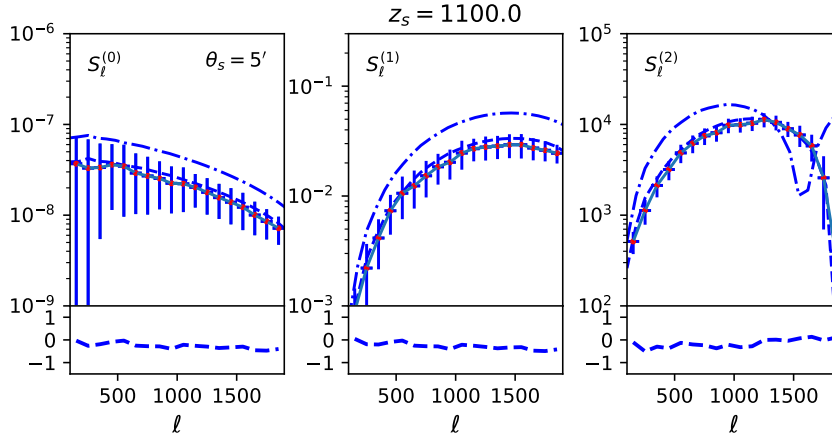
Figure 6. Same as Figure-5, but for $\theta_s = 5.0'$.

impact on theoretical predictions. Over the entire range of smoothing angular scales θ_s and angular harmonics ℓ studied we haven't found any significant departure from theoretical predictions. We have used $N_{\rm side} = 4096$ in our study. The skew-spectra are sensitive to the ℓ_{max}. We have included all modes up to $\ell_{max} = 2000$ in our calculation in our theoretical predictions. To be consistent we have also filtered all modes higher than ℓ_{max} while processing the numerical simulations. We have also tested the impact of retaining the lower harmonics in our numerical evaluation by filtering out these modes from the maps as well as keeping them in while computing the skew-S_ℓs. We didn't find any statistically significant difference in our final results. The flexibility and simplicity with which the skew-spectra can be evaluated gives a very efficient to study the spectra in a mode-by-mode manner thus providing a greater handle on dealing with any possible systematics. Notice that the perturbative reconstruction of the MFs requires the expansion parameter σ_0 introduced in Eq.(4) to be small for the series to be convergent but, the three skew-spectra can also be used as independent estimators
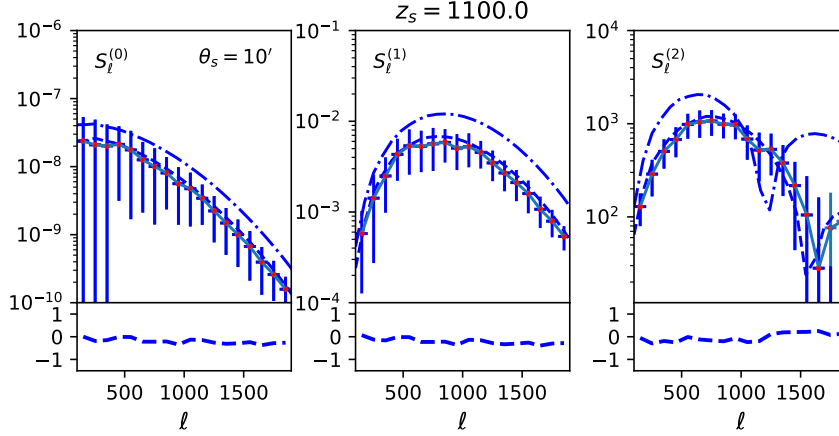
Figure 7. Same as Figure-5, but for $\theta_s = 10.0'$.

of non-Gaussianity and a method of effective data compression in their own right. This makes them attractive even when the series in Eq.(7) is divergent at smaller angular scales. The convergence of the series expansion and its implications were considered in (Petri et al. 2013) to some extent. However, a detailed study is needed for a realistic assessment as a function of various survey parameters.

(ii) **Skew-spectra from CMB maps:** In Fig.-5-Fig.7 the generalised spectra $S^{(0)}$ (left panel), $S^{(1)}$ (middle panel) and $S^{(2)}$ (right panel) are plotted for redshift $z_s = 1100.0$. The convergence maps are inferred from CMB observations. The variance or skew-spectra increases with redshift or the depth of the survey. To reduce the scatter in our estimates we have used binning with bin-size $\Delta_\ell = 100$. While in Fig.-5 the smoothing angular scale is sized at $\theta_s = 2'$, in Fig.-6 and Fig.-7 this angular scale is fixed respectively at $\theta_s = 5'$ and $10'$. The dot-dashed lines correspond to Born approximation. The dot-dashed lines in each panel include the post-Born corrections. The important difference of the CMB skew-spectra with the ones at lower redshifts is the significance of post-Born correction in modelling of non-Gaussianity. The post-Born correction is non-linear and it is known to generate a non-negligible bispectrum of the convergence (Marozzi et al. 2016; Pratten & Lewis 2016). Our study confirms that the post-Born contributions to the bispectrum can significantly change the shape predicted for the skew-spectrum from the large-scale structure non-linearities alone. This is more obvious in the right panels where the generalised skew-spectrum $S_\ell^{(2)}$ changes a signature from positive at lower ℓ to negative at higher ℓ.

(iii) **Skew-spectrum from cross-correlating two different tomographic bins:** In addition to studying the skew-spectra from individual tomogrpahic bins we have also cross-correlated different bins to construct the skew-spectra. Indeed the link to morphology no longer exists but this gives us a clue about how these estimators are correlated. It can also be argued, irrespective of morphological connection, that these estimators provide an efficient tool for data compression.

In Fig.-8 and Fig.-9 we show the cross skew-spectra of two tomographic bins $z_s = 1.0$ and $z_s = 2.0$. We have fixed $\theta_s = 10'$ in each of these plots. The error-bars are computed using the fluctuations within a bin. The bin size is $\Delta_\ell = 100$. In each case we find that the analytical and numerical predictions agree within 2σ in the cosmic variance limited case.

In Fig.10 and Fig.11 we plot the skew-spectra constructed from κ maps inferred from CMB observations at $z_s = 1100$ (denoted as $\kappa_{\rm LSS}$) and cross-correlated against convergence map at $z_s = 1.0$ (denoted as κ_1). In Fig.10 we plot the skew-spectra related to $\langle \kappa_{\rm LSS}^2 \kappa_1 \rangle$ and in Fig.11 the skew-spectra corresponding to $\langle \kappa_{\rm LSS} \kappa_1^2 \rangle$ is being plotted. Compared to the low-z cases the theoretical predictions for $\langle \kappa_1 \kappa_{\rm LSS}^2 \rangle$ are found to significantly over-estimate the simulation results. This is true to a lesser extent for $\langle \kappa_1^2 \kappa_{\rm LSS} \rangle$. This may be related to the fact that the simulation using a Gaussian realisations at higher redshifts $z_s > 7.1$ which may lead to suppression of non-Gaussinity. The descrepency becomes, however, not so significant when compared with the scatter within the beam.

(iv) **Euclid-like Mask, Noise and Skew-spectrum:** In Figure-12 we show the three skew-spectra for a Euclid-like survey. We use a "pseudo *Euclid*" mask. To construct this mask all pixels lying within $22\,\mathrm{deg}$ of either the galactic or ecliptic planes are discarded. Such
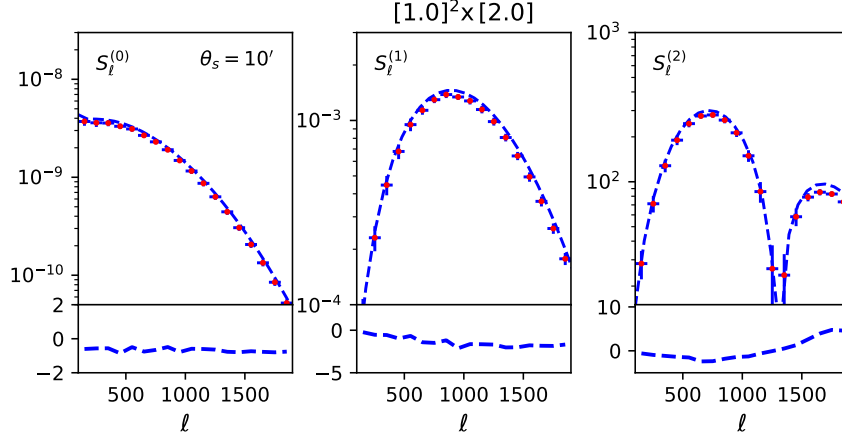
Figure 8. We have chosen two redshift bins $z_1 = 1.0$ and $z_2 = 2.0$. From left to right we show results for the skew-spectra $S_\ell^{(0)}$, $S_\ell^{(1)}$ and $S_\ell^{(2)}$ as a function of ℓ. The smooth curves represent theoretical predictions where as data points represent estimates from the simulations. These generalised skew-spectra are defined in Eq.(15a)-Eq.(15c). In each panel we show $\langle \kappa_1^2 \kappa_2 \rangle$ (in our notation, $\kappa_1 = \kappa(z_1)$) and $\kappa_2 = \kappa(z_2)$) and $\langle \kappa_1^2 \kappa_2 \rangle$ for two different smoothing angular scales $\theta_s = 10'$. One single all-sky map was used to construct the skew-spectra. No noise was included in our study.

a mask leaves $14,490 \deg^2$ of the sky making i.e. fraction of the sky covered $f_{\rm sky} \approx 0.35$ (see (Munshi et al. 2020) for more detailed discussion). We use maps with source plane fixed at $z_s = 1.0$. In each panel the upper curves correspond to the all-sky S_ℓ estimates and the lower curves correspond to the pseudo-$\hat{S}_\ell$s (see Eq.(20a)). To compute the scatter one realization of the map was considered. To simulate noise we have included a source density of $n_s = 30 \, {\rm arcmin}^{-2}$. However, we found that the Euclid-type noise do not produce any significant effect on the scatter. To increase the effect of noise we have artificially increased the level of noise by a factor of two.

8 CONCLUSIONS AND FUTURE PROSPECTS

The high signal-to-noise of the skew-spectra and the flexibility with which they can be implemented is rather encouraging. The accuracy of the fitting function in reproducing the numerical simulations opens up several possible avenues of research.

Perturbative contributions from trispectrum: Beyond the leading-order non-Gaussian corrections, that come from bispectrum, the four generalised kurtosis parameters $K^{(0)}$, $K^{(1)}$, $K^{(2)}$, and $K^{(3)}$, play an important role in perturbative reconstruction of the morphology of a non-Gaussian field. These are the contributions denoted as $\delta V_k^{(3)}$ in Eq.(4). These kurtosis parameters were generalised to kurtosis-spectra in a manner similar to the generalisation of the skewness parameters to the skew-spectrum (Munshi et al. 2016). The kurtosis-spectra were used in the context of CMB studies and sources of non-Gaussianity studied include the primordial non-Gaussianity as well as lensing induced non-Gaussianity. Extension of our results to incorporate higher-order terms in the context of weak lensing studies for gravity induced non-Gaussianity will require an analytical model of the trispectrum. The analytical expression for the perturbative trispectrum is more involved and will require a dedicated study. Various other options to include the validity domain of the perturbative expression include Effective Field Theoretic (EFT) or Halo Model (HM) based approaches. We plan to extend our results in future in these directions.

Study of morphology from shear maps: In our study we have extracted the generalised skew-spectra directly from convergence maps. This requires an intermediate step of map making from shear maps. However, our method can also be generalised to directly deal with shear maps by implementing an Electric/Magnetic (E/B) decomposition of shear maps. The PSL approach can be generalised to deal with such a decomposition and deal with arbitrary mask. This will be useful in bypassing the map making process needed for
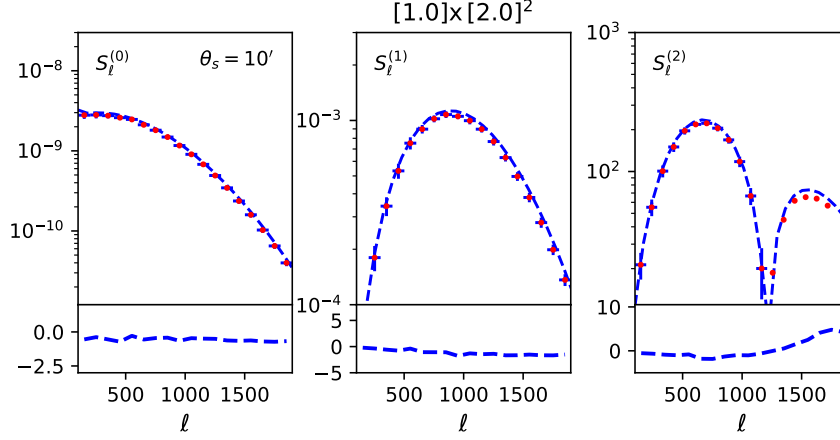
Figure 9. Same as Figure-8 but the skew-spectra associated with $\langle \kappa_1 \kappa_2^2 \rangle$ is being plotted.
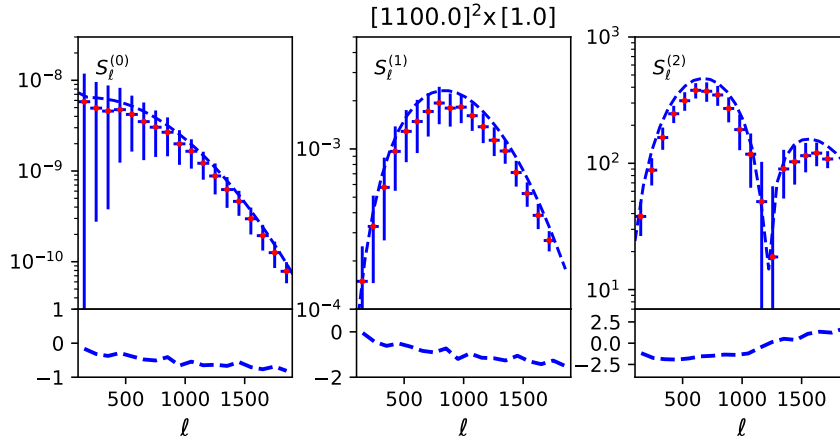

Figure 10. Same as Figure-8 but for $z_1 = 1100$ and $z_2 = 1.0$. For $z_s = 1100$ the κ is being inferred from CMB observations.

generating convergence maps. This will also be important dealing directly with spurious magnetic or B mode generated due to unknown systematics.

Likelihood Analysis and Covariance Matrix: Any cosmological parameter inference using MFs would require a detailed characterization of covariance matrix of the skew-spectra. The calculation of covariance matrices were presented in (Munshi et al. 2011) using a simplistic approach that is valid in the noise dominated regime i.e. in the limit of vanishing non-Gaussianity. This is achieved by
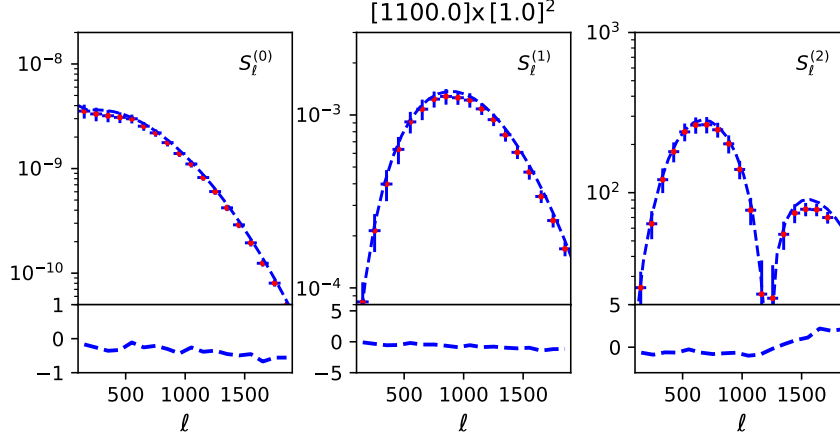
Figure 11. Same as Figure-10 but for $z_1 = 1.0$ and $z_2 = 1100.0$.
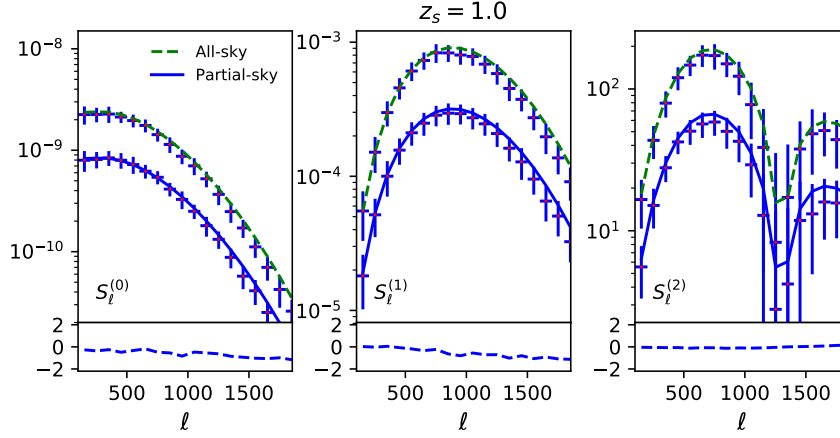
Figure 12. We show the three skew-spectra for a Euclid-like survey. In our study we use a "pseudo Euclid" mask. All pixels lying within $22 \deg$ of either the galactic or ecliptic planes are discarded while constructing the mask. Which leaves $14,490 \deg^2$ of the sky making fraction of the sky covered $f_{\rm sky} \approx 0.35$ (see (Munshi et al. 2020) for more detailed discussion). The source plane is fixed at $z_s = 1.0$. In each panel the upper curves correspond to the all-sky S_ℓ estimates and the lower curves correspond to the pseudo-$\hat{S}_\ell$s (see Eq.(20a)). One realization of the all-sky maps were considered. To simulate noise we have included a source density of $n_s = 30 \, {\rm arcmin}^{-2}$. With Euclid type noise the error-bars are nearly identical to what was presented in Figure-2. To amplify the effect of noise we have artificially increased the noise by a factor of two.

ignoring the contributions from all higher-order non-Gaussianity. While such approximate treatment may be enough to deal with present generation of surveys, stage-IV observation including the *Euclid* will map the sky with higher signal-to-noise and may require a more accurate modelling is thus required.

Intrisic Allignment: The intrinsic alignment (IA) remains a major contamination to the gravity induced secondary non-Gaussianity. Analytical modelling of IA is challenging though quite a few physically motivated models can capture certain aspects of the non-Gaussianity induced by IA (Vlah, Chisari, Schmidt 2019). Typically at the level of bispectrum, IA is expected to contribute at 10% of the gravity induced non-Gaussianity. Using the skew-spectra introduced here it will be possible to compute the corrections to the

morphological change induced by IA. In addition optimal weights combined with a match filtering approach can in effect may lead to separation of the two sources.

Betti number and other topological estimators: The MF were recently generalised in a series of paper to Tensorial Minkowski Functionals (TMF) in 2D and 3D as well as in redshift-space (Appelby et al. 2017; Chinangbam 2017). The results presented here will be extended to the case of TMF for a 3D convergence maps in future. Other estimators related to morphology of cosmological fields have recently attracted attention, such as the Betti numbers (Pranav et al. 2019). Reconstruction techniques used here can be useful in these contexts.

Optimality and Flexibility of implementation: We have not included optimal weighting in our estimator as the signal-to-noise is very high for low source redshift studies. This is not completely true for the studies involving κ maps. Various methods can be used to improve the signal-to-noise including a Wiener or "Wiener-like" filtering of κ maps (Ducout et al. 2013). Alternatively following (Munshi & Heavens 2010) the generalised skew-spectra can include optimal weights that inherits a match filtering approach. However, there is a price to pay as the direct links to morphology will be lost and the estimators will have less flexibility in dealing with partial sky coverage as the PSL developed in our study will not be valid.

Beyond ΛCDM scenarios : Though we have only discussed the gravity induced secondary non-Gaussianity as a possible source of non-Gaussianity, many other source of non-Gaussianities can also be included in our framework e.g. primordial non-Gaussianity or non-Gaussianity induced by active source of perturbations or topological defects can also be studied using their impact on morphology of convergence maps. Many modified gravity theories predict a different form of bispectrum compared to General Relativity and their impact on morphology can be studied using the formalism developed here (Munshi, McEwen 2020).

REFERENCES

Abott et al. The Dark Energy Survey Collaboration, 2016, Phys. Rev. D, 94, 022001 [`arXiv/1507.05552`]

Appleby S., Chingangbam P., Park C., Hong S. E., Kim J., Ganesan V., 2017, JCAP, 12, 023 `arXiv/1805.08752`

Barber A. J., Munshi D., Valageas P., 2004, MNRAS, 347, 667 [`astro-ph/0304451`]

Bernardeau F., Colombi S., Gaztanaga E., Scoccimarro R., 2002, Phys.Rept. 367, 1, [`astro-ph/0112551`].

Castro P. G., Heavens A. F., Kitching T. D., [`astro-ph/0503479`]

Canavezes A., et al., 1998, MNRAS, 297, 777 [`astro-ph/9712228`]

Coles P., 1988, MNRAS, 234, 509 [`ADS`]

Chingangbam P., Yogendran K. P., Joby P. K., Ganesan V., Appleby S., Park C., `arXiv/1707.04386`

Clifton T., Ferreira P.G., Padilla A., Skordis C., 2012, Physics Reports 513, 1, 1 [`astro-ph/1106.2476`]

Desjacques V., Jeong D., Schmidt F., [`arXiv/1611.09787`]

Ducout A., Bouchet F., Colombi S., Pogosyan D. , Prunet S., 2013, MNRAS, 429, 2104 [`arXiv/1209.1233`]

Drinkwater, M. J., Jurek, R. J., Blake, C., et al. 2010, MNRAS, 401, 14, [`astro-ph/0911.4246`]

eBOSS Collaboration, 2020 [`arXiv/2007.08991`]

Eisenstein, D. J., Weinberg, D. H., Agol, E., et al. 2011, AJ, 142, 72, [`astro-ph/1101.1529`]

Gorski K. M., Hivon E., Banday A. J., Wandelt B. D., Hansen F. K.,
 Reinecke M., Bartelman M., 2005, ApJ, .622, 759 [`astro-ph/0409513`]

Laureijs R., Amiaux J., Arduini S., et al. 2011, ESA/SRE(2011)12

Gott J. R., Mao S., Park C., Lahav O., 1992, ApJ, 385, 26 [`ADS`]

Gil-Marín H., Wagner C., Fragkoudi F., Jimenez R., Verde L., 2012, JCAP, 02, 047 [`arxive/1111.4477`]

Gleser L., Nusser A., Ciardi B., Desjacques V., 2006, MNRAS, 370, 1329, [`astro-ph/9710185`]

Gott J. R., Mellot A. L., Dickinson M., 1986, ApJ, 306, 341 [`ADS`]

Gott J. R., et al., 1989, ApJ, 340, 625 [`ADS`]

Harnois-Déraps, J.; Munshi, D.; Valageas, P.; van Waerbeke, L.; Brax, P.; Coles, P.; Rizzo, L. 2015, MNRAS, 454, 2722 `arXiv/1506.06313`]

Hadwiger H. 1959, Normale Koper im Euclidschen raum und ihre topologischen and metrischen Eigenschaften, Math Z., 71, 124

Hikage C., Coles P., Grossi M., Moscardini L., Dolag K., Branchini L., Matarrese S. 2008, MNRAS,385,1513 [`astro-ph/0711.3603`]

Hikage C., et al., 2002, Publ. Astron. Soc. Jap., 54, 707 [`astro-ph/0207377`]

Hikage C., Komatsu E., Matsubara T., 2006, ApJ, 653, 11 [`arxive/0607284`]

Hikage C., et al., 2008, MNRAS, 385, 1613-1620 [`arXiv/0711.3603`]

Hikage C., et al., 2008, MNRAS, 389, 1439 [`arxive/0802.3677`]

Joyce A., Jain B., Khoury J., Trodden M., 2015, Physics Reports, 568, 1 [`astro-ph/1407.0059`]

Kerscher M., et al., 2001, A & A, 373, 1-11 [`astro-ph/0101238`]

Kuijken K., Heymans C., Hildebrandt H., et al. 2015, MNRAS, 454, 3500

Laureijs R., Amiaux J., Arduini S., et al. 2011, ESA/SRE(2011)12

Lesgourgues J., Pastor S., 2006, Phys.Rept., 429, 307, [`astro-ph/1610.02956`]

Marozzi G., Fanizza G., Di Dio E., Durrer R., 3016, JCAP, 1609, 028 [`arXiv/1605.08761`]

Matsubara T., Jain B., 2001, ApJ, 552, L89 [`astro-ph/0009402`]

Melott A. L., 1990, Phys. Rep., 193, 1 [`ADS`]

Moore B., et al., 1992, MNRAS, 256, 477 [`ADS`]

Munshi D., 2000, MNRAS, 318, 145 [`astro-ph/0001240`]

Munshi D., Jain B., 2000, MNRAS, 318, 109 [`astro-ph/9911502`]

Munshi D. , Valageas P., Barber A. J., 2004, MNRAS 350, 77 [`astro-ph/0309698`]

Munshi D., Valageas P., van Waerbeke L., Heavens A., 2008, Phys.Rept.462, 67 [`astro-ph/0612667`]

Munshi D., Jain B., 2001, MNRAS, 322, 107 [`astro-ph/9912330`]

Munshi D., Heavens A., 2010, MNRAS, 401, 2406, [`astro-ph/0001240`]

Munshi D., Smidt J., Joudaki S., Coles P., 2011, [`arXiv/1002.2089`]

Munshi D., Smidt J., Heavens A., Coles P., Cooray A., 2011, MNRAS, 411, 2241 [`astro-ph/0001240`]

Munshi D., Heavens A., Cooray A., Smidt J., Coles P., Serra P., 2011, MNRAS, 412, 1993 [`arxive/0910.3693`]

Munshi D., Heavens A., Coles P. 2011, MNRAS, 411, 2161 [`astro-ph/1002.2089`]

Munshi D., van Waerbeke L., Smidt J., Coles P., 2012, MNRAS, 419, 536 [`arXiv/1103.1876`]

Munshi D., Kitching T., Heavens A., Coles P. MNRAS, (2011), 416, 629 [`astro-ph/1012.3658`]

Munshi D., Hu B., Matsubara T., Coles P., Heavens A., 2016, JCAP, 04, 056 [`arXiv/1309.4460`]

Munshi D., Namikawa T., Kitching T. D., McEwen J. D., Takahashi R., Bouchet F. R., Taruya A., Bose B., 2020, MNRAS, 493, 3985 [`arXiv/1910.04627`]

Munshi D., McEwen J. D., 2020, [`arXiv/2004.07021`]

Munshi D., Namikawa T., Kitching T. D., McEwen J. D., Bouchet F. R., [`arXiv/2006.12832`]

Munshi D., Namikawa T., Kitching T. D., McEwen J. D., Bouchet F. B., [`arXiv/1905.05697`]

National Research Council. 2010. New Worlds, New Horizons in Astronomy and Astrophysics. The National Academies Press. https://doi.org/10.17226/12951.

Namikawa T¿, Bose B., Bouchet F. R.,Takahashi R., Taruya A., [`arxiv/1812.10635`]

Natoli P., et al., 2010, 408, 3, 1658-1665 [`arxive/0905.4301`]

Novikov D., Schmalzing J., Mukhanov V. F., 2000, A & A, 364 [`arxive/0006097`]

Park C., et al., 2005, ApJ, 633, 11 [`astro-ph/0507059`]

Planck Collaboration, 2016, A&A 594 A13, [`astro-ph/1502.1589`]

Planck Collaboration, 2016, A&A, 594A, 17, [`arxive/1502.01592`]

Planck Collaboration, 2014, A&A, 571, A16, [`astro-ph/1303.5076`]

Planck Collaboration, [`astro-ph/1807.06209`]

Petri A., Haiman Z., Hui L., May M., Kratochvil J. M., 2013, PRD, 88, 123002 [`arXiv/1309.4460`]

Pratten G., Lewis A., 2016, JCAP, 08, 047, 2016, JCAP 1608, 08, 047 [`arXiv/1605.05662`]

Pranav P., van de Weygaert R., Vegter G., B. Jones J. T., Adler R. J., Feldbrugge J., Park C., Buchert T., Kerber M. 2019, MNRAS, 485, 3, 4167, [`arXiv/1812.07310`]

Sato J., Takada M., Jing Y. P., Futamase T., 2001, ApJ, 551L,5 [`astro-ph/0104015`]

Scoccimarro R, Frieman J. A., 1999, ApJ, 520, 35 [`astro-ph/9811184`]

Schmalzing J., Górski K. M., 1998, MNRAS, 297, 355 [`astro-ph/9710185`]

Schmalzing J., Diaferio A., 2000, MNRAS, 312 [`astro-ph/9910228`]

Taruya A., et al., 2002, ApJ, 571, 638 [`astro-ph/0202090`]

Tomita H., 1986, Progr.Theor.Phys, 76, 952

Takahashi R., Hamana T., Shirasaki M., Namikawa T., Nishimichi T., Osato K., Shiroyama K., 2017, ApJ, 850, 24 [`arXiv/1706.01472`]

Tyson J. A., Wittman D. M., Hennawi J. F., Spergel D. N. 2003, Nuclear Physics B Proceedings Supplements, 124, 21

Valageas P. , Munshi D., Barber A. J., 2005, MNRAS. 356, 386 [`astro-ph/0402227`]

Valageas P., Barber A. J., Munshi D., 2004, MNRAS, 347, 654 [`astro-ph/0303472`]

Vlah Z., Chisari N. E., Schmidt F., [`arXiv/1910.08085`]

Weiss A. J., Schneider A., Sgier R., Kacprzak T., Amara A., Refregier A., [`arXiv/1905.1136`]

Mandelbaum, R. 2018, ARA&A, 56, 393 [`arXiv/1710.03235`]

Bartelmann M., Schneider P., Phys.Rept, 340, 291,2001 [`astro-ph/9912508`]

Kilbinger M., Rep. Prog. Phys. 78 (2015) 086901 [`astro-ph/9912508`]

Gott, J. R. III, Park, C., Juszkiewicz, R., Bies, W. E., Bennett D. P., Bouchet, F. R.; Stebbins, A. 1990, ApJ, 352, 1G [`ADS`]

Planck Collaboration, 2019, [`arXiv/1905.05697`]